Single n^+-i-n^+ InP nanowires for highly sensitive terahertz detection

OPEN ACCESS

Made open access 2 March 2017

IOP Publishing

Nanotechnology

Nanotechnology **28** (2017) 125202 (9pp)

https://doi.org/10.1088/1361-6528/aa5d80

Single n^+-i-n^+ InP nanowires for highly sensitive terahertz detection

Kun Peng[1], Patrick Parkinson[2], Qian Gao[1], Jessica L Boland[3], Ziyuan Li[1], Fan Wang[4], Sudha Mokkapati[5], Lan Fu[1,6], Michael B Johnston[3,6], Hark Hoe Tan[1] and Chennupati Jagadish[1]

[1] Department of Electronic Materials Engineering, Research School of Physics and Engineering, The Australian National University, Canberra, ACT 2601, Australia
[2] School of Physics and Astronomy and the Photon Science Institute, University of Manchester, Manchester, M13 9PL, United Kingdom
[3] Department of Physics, University of Oxford, Clarendon Laboratory, Oxford, OX1 3PU, United Kingdom
[4] ARC Centre of Excellence for Nanoscale BioPhotonics (CNBP), Faculty of Science, Macquarie University, Sydney, NSW 2109, Australia
[5] School of Physics and Astronomy, Cardiff University, Cardiff, CF24 3AA, United Kingdom

E-mail: lan.fu@anu.edu.au and michael.johnston@physics.ox.ac.uk

Received 16 November 2016, revised 28 January 2017
Accepted for publication 1 February 2017
Published 20 February 2017

Abstract

Developing single-nanowire terahertz (THz) electronics and employing them as sub-wavelength components for highly-integrated THz time-domain spectroscopy (THz-TDS) applications is a promising approach to achieve future low-cost, highly integrable and high-resolution THz tools, which are desirable in many areas spanning from security, industry, environmental monitoring and medical diagnostics to fundamental science. In this work, we present the design and growth of n^+-i-n^+ InP nanowires. The axial doping profile of the n^+-i-n^+ InP nanowires has been calibrated and characterized using combined optical and electrical approaches to achieve nanowire devices with low contact resistances, on which the highly-sensitive InP single-nanowire photoconductive THz detectors have been demonstrated. While the n^+-i-n^+ InP nanowire detector has a only pA-level response current, it has a 2.5 times improved signal-to-noise ratio compared with the undoped InP nanowire detector and is comparable to traditional bulk THz detectors. This performance indicates a promising path to nanowire-based THz electronics for future commercial applications.

Supplementary material for this article is available online

Keywords: InP nanowire, axial doping, terahertz, optoelectronics, photonics, detector

(Some figures may appear in colour only in the online journal)

Introduction

Over the past decade, terahertz time-domain spectroscopy (THz-TDS) has emerged from being a laboratory-based technique to find a number of industrial and commercial applications [1]. In particular, materials characterization, including nanomaterials [2], pharmaceuticals [3], bio-molecules [4], process monitoring [5] and homeland security fields [6, 7] have all been shown to benefit from using THz-TDS as a contact-free, non-ionizing and molecular-vibration sensitive probe. As part of this development, photoconductive (Auston-type [8]) THz emitter and detector technology has advanced via the introduction of ion-damaged [9] or low–temperature grown [10] III–V semiconductor materials, which possess fast photoconductivity rise times, short carrier lifetimes and high carrier mobilities, and complex antenna geometries [11] for broadband operation. However, the manufacture of photoconductive emitters or detectors remains limited and at high cost, owing to the challenges associated with the production of semiconductors that exhibit these desirable optoelectronic

[6] Author to whom any correspondence should be addressed.

properties. Furthermore, current THz-TDS techniques present many challenges for miniaturization due to the constraints posed by sub-millimeter wavelengths. To overcome this limitation, a miniaturized or on-chip THz spectrometer has been proposed, which could lead to improvements in near-field spectroscopy for sub-wavelength THz imaging and the application of THz characterization to microscopic samples [12, 13]. One way to develop simple, low-cost, highly integrable emitter and detector structures for such advanced applications is through the use of quasi-1D semiconductor nanowires [14] as the active element.

Semiconductor nanowire detectors for THz applications have been demonstrated using a number of approaches (such as plasma-wave detectors based on nanowire field-effect transistors [15–17]). Nevertheless, for the most powerful THz-TDS applications, photoconductive antenna-based nanowire detectors are demanded. We have previously shown that single GaAs/AlGaAs nanowires can provide many of the desired properties [18], suitable for use as sensitive detectors in THz-TDS. More recently, we have reported that nominally undoped InP single-nanowire photoconductive detectors with optimized antenna structure have excellent sensitivity and broadband performance [19], approaching that of conventional bulk Fe^{+} ion-implanted InP [20] photoconductive antennas. While it might be assumed that the nanoscale material volume of nanowires would present a disadvantage to their use for THz detection, we have shown that the advantages in signal-to-noise ratio [20] and dynamic range [21] gained from a greatly enhanced on–off ratio can outweigh the reduction in signal size. Having previously optimized both the active material system and antenna, we now seek to further improve the efficiency of nanowire detectors to compete with that of conventional devices, by selectively doping the nanowire to optimize the contact design. Thus coupled with a variety of material synthesis methods [22], low material cost and opportunities for high density integration, such nanowire detectors are of great promise for a myriad of THz spectroscopy applications.

In conventional photoconductive THz emitters and detectors, contact quality is known to play a significant role in determining device performance [23]. Lower contact resistance leads to higher output power in photoconductive emitters; similarly, for effective detection, Ohmic contacts are essential to ensure maximum detection sensitivity [24]. Nominally undoped InP single-nanowire detectors [19] have been shown to exhibit a clear Schottky interface between the nanowire and metal contact, thereby reducing sensitivity. It is therefore important and necessary to create high-quality Ohmic contacts to further improve nanowire photoconductive detectors. Common techniques to form Ohmic metal–semiconductor contacts include thermal alloying [25, 26] and ion-implantation [27] at the contact region. Unfortunately, these methods are not suitable for use with semiconductor nanowire devices, as the former can lead to thermal decomposition, while the latter is extremely challenging and risks material damage. A careful metal choice can help [26], for example, non-annealed contacts, such as Ti/Au contacts, have been widely used for the low-temperature grown GaAs photoconductive THz antennas to achieve Ohmic behavior [26, 28, 29]. However, the very limited contact surface area for single-nanowire devices leads to significant device-to-device variation in the resultant contact quality. In this work, we take advantage of the ease of designing and characterizing axially modulated doping in nanowires to grow n^{+}-i-n^{+} axial structures. By making electrical contact to the highly doped end regions of the nanowire, we aim to reduce contact resistance while maintaining the high sensitivity of the nanowire architecture. While the n^{+}-i-n^{+} structures have been previously reported for planar photodetectors [30] and, more recently, GaN-based nanowire photodetectors [31, 32], its use for photoconductive devices has not yet been reported.

In this paper, we focused on growth and characterization of the n^{+}-i-n^{+} structures, along with fabrication and testing of integrated photoconductive detectors based on InP single nanowires. It is noted that effective characterization of spatially varying carrier densities in a single nanowire is typically highly challenging due to the small volumes of material involved and thus limited techniques. As such, we used a newly developed optical technique [33] to measure the local carrier density with diffraction-limited resolution. By correlating these measurements with 2- and 4-terminal contact electrical studies, we evaluated the effectiveness of the axially modulated doping approach. Finally, the fabricated n^{+}-i-n^{+} InP single-nanowire photoconductive detectors are incorporated in a THz-TDS system, where they are shown to be superior alternatives to undoped InP single-nanowire detectors. We also demonstrated that despite their nano-size active volumes, n^{+}-i-n^{+} single InP nanowire detectors perform comparably to conventional bulk InP THz detectors, exhibiting great promise for further implementation in industrial THz systems. This work opens a new avenue for design and improvement of single-nanowire photoconductive detectors for commercial THz applications, which may be also applicable for design and optimization of highly efficient single-nanowire photoconductive emitters. With the single-nanowire THz electronics developed via this approach, we are one step closer to realizing a high-performance on-chip THz-TDS spectrometer [12, 13].

Experiment

All InP nanowires studied in this work were grown on bulk (111)A InP substrates, using a selective-area metal organic vapor phase epitaxy (SA-MOVPE) technique in a commercial MOVPE reactor (AIXTRON 200/4). The undoped InP nanowires were grown following a previously reported approach [33, 34], which has been shown to produce unintentionally n-type doped, defect-free and pure wurtzite (WZ) InP nanowires. The unintentional doping in these undoped InP nanowires can be attributed to the background impurities in the MOVPE precursors [35]. Prior to the nanowire growth, a 30 nm-layer SiO_2 mask was first deposited on a (111)A InP substrate, patterned by an electron beam lithography system and selectively etched by using buffered hydrofluoric acid solution to create hexagonal arrays of open circles on the SiO_2

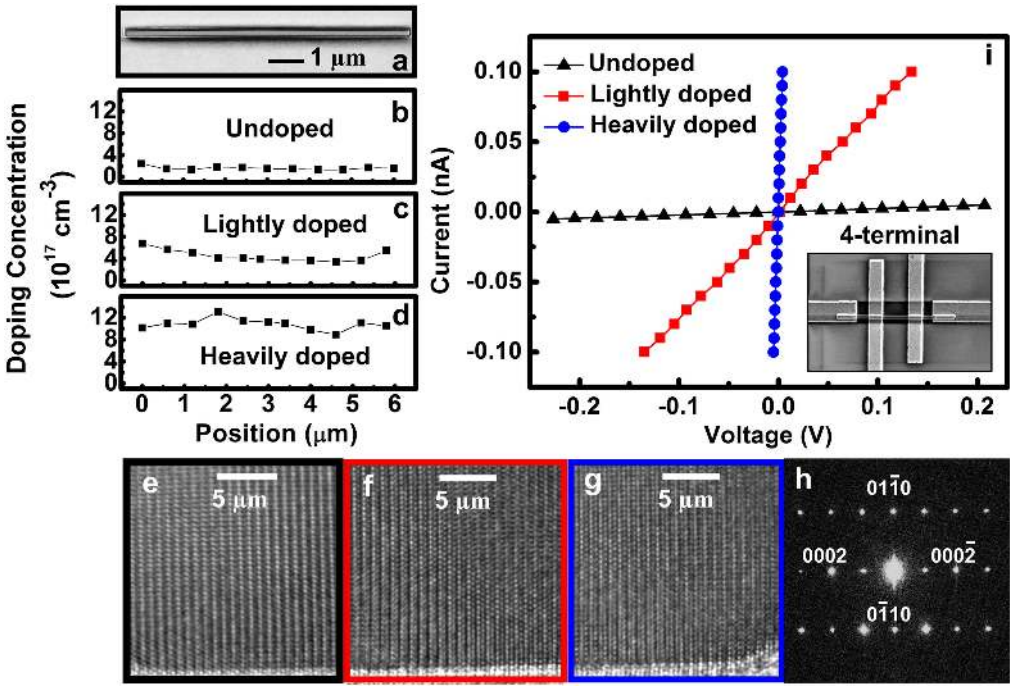

Figure 1. (a) A SEM image of a typical single InP nanowire studied in this work. Doping profiles of single InP nanowires with (b) unintentional, (c) light and (d) heavy doping measured using the technique described in [33]. (e)–(g) TEM images taken along [$\bar{2}$110] zone axis from InP nanowires corresponding to (b)–(d). (h) Selected area electron diffraction pattern of a typical Si-doped InP nanowire confirming the WZ phase. The images from (e)–(h) show all nanowires have a WZ structure and are free of stacking faults. (i) Dark *I*–*V* characteristics of the InP nanowires from the same growths as (b)–(d) based on a 4-terminal contact measurements (inset: SEM image of a single InP nanowire device having four-terminal contacts).

mask. The circle diameter was ~200 nm with a pitch of 800 nm. The patterned substrates were then loaded into a horizontal-flow low-pressure MOVPE system for nanowire growth. The undoped InP nanowires were grown at 730 °C for 40 min with trimethylindium and phosphine precursors at a flow rate of 6.1×10^{-6} and 4.9×10^{-4} mol min^{-1} respectively. For intentional n^+ doping calibration, gaseous silane (SiH_4) at varied flow rates was introduced during nanowire growth, with all other parameters kept unchanged, to produce uniformly silicon (Si)-doped, n-type [36] InP nanowires with different doping concentration. In order to grow the n^+-i-n^+ nanowire structure, SiH_4 gas was introduced at the beginning of the nanowire growth, shut off during growth of the i section, and introduced again for the rest of nanowire growth.

Results

To achieve appropriate doping in the n^+-i-n^+ single InP nanowires, the relationship between nanowire growth, doping characteristics and resultant device contact quality of undoped and uniformly n-doped InP nanowires with different dopant concentrations were firstly studied. Both undoped and doped InP nanowires were found to have a high structural uniformity, with a diameter in the range of 220–260 nm and a length of 8–12 μm. A typical scanning-electron-microscopy (SEM) image of a single InP nanowires studied in this work is shown in figure 1(a). Doping profiles of single InP nanowires for various growth conditions were measured using a novel optical technique described in [33], which combines both power-dependent photoluminescence (PL) and time-resolved PL (TRPL) measurements. Details of this technique and measurements are provided in the supporting information is available online at stacks.iop.org/NANO/28/125202/mmedia. Figures 1(b)–(d) show the doping profiles along the length of single InP nanowires under three growth conditions: with SiH_4 flow rates of 0, 5.1×10^{-8} and 3.1×10^{-7} mol min^{-1}, introduced uniformly during growth. These growth conditions lead to doping concentration values of $(0.16 \pm 0.04) \times 10^{18}$ cm^{-3}, $(0.45 \pm 0.09) \times 10^{18}$ cm^{-3} and $(1.08 \pm 0.29) \times 10^{18}$ cm^{-3}, which we refer to as undoped, lightly-doped and heavily-doped InP nanowires, respectively. Since inhomogeneity in a nanowire ensemble is known to lead to variations in doping concentrations among nanowires, statistical measurements were performed to evaluate an average doping level for each growth condition (data are provided in supporting information). The average doping concentration was determined to be 0.17×10^{18} cm^{-3} for the undoped InP nanowires and 0.49×10^{18} cm^{-3} for the lightly doped nanowires; both of them show a uniform doping profile along the length of nanowires. The heavily-doped nanowires show some variations in doping concentration among nanowires with values ranging from 1.08×10^{18} cm^{-3} to 1.76×10^{18} cm^{-3}, while exhibiting a slight non-uniform doping profile along the length of single nanowires. The effect of Si doping on crystal defect evolution in these InP nanowires was examined by transmission electron

microscopy (TEM). Figures 1(e)–(g) display the TEM images for the undoped, lightly-doped and heavily-doped InP nanowires, taken from the same growth batch as described in figures 1(b)–(d). The TEM images show a pure WZ structure (see figure 1(h)) with no stacking faults observed for all nanowires. The presence of Si in these InP nanowires was found to be below the energy-dispersive x-ray detection limit (~0.3 atomic percent, equivalent to $1 \times 10^{19}\,\mathrm{cm}^{-3}$), in agreement with their evaluated doping concentrations.

These InP nanowires were then fabricated into single nanowire devices for both 2-terminal and 4-terminal current–voltage (*I–V*) measurements. The device geometry is shown as an inset image in figure 1(i) (details of the device fabrication process can be found in supporting information). 2-terminal measurements reveal the overall behavior (including contact type—Schottky or Ohmic—and quality) of the nanowire device; whereas 4-terminal measurements allow the accurate measurement of nanowire resistivity without the influence of contact resistance. Figure 1(i) displays the room-temperature 4-terminal dark *I–V* characteristics of the undoped, lightly-doped and heavily-doped InP single nanowires, showing a clear decrease in nanowire resistance with increasing SiH_4 flow during growth. These results are consistent with their doping concentration analysis, as shown in figures 1(b)–(d). The resistance between the 2 internal contacts (separated by 1.5 μm), obtained via the 4-terminal measurements was found to be approximately $4 \times 10^{10}\,\Omega$, $1 \times 10^{9}\,\Omega$ and $2 \times 10^{5}\,\Omega$ for the undoped, lightly-doped and heavily-doped InP nanowires respectively, one or two orders of magnitude smaller than that obtained in their 2-terminal measurements (see online supplementary information). This difference between measurements highlights the huge influence of contact resistances on nanowire device performance. It is noted that, in 2-terminal measurements, *I–V* characteristics for devices from undoped and lightly-doped single InP nanowires show typical Schottky behaviors, whereas the *I–V* characteristics for devices from heavily-doped single InP nanowires show a near-Ohmic behavior, indicating that Si doping above $\sim 1 \times 10^{18}\,\mathrm{cm}^{-3}$ can create low-resistance contacts for InP nanowire devices [36].

Utilizing this understanding of the relationship between contact resistance and nanowire doping from the 2-terminal and 4-terminal *I–V* measurements, n^+-i-n^+ InP nanowires were designed to produce Ohmic contacts. To grow an n^+-i-n^+ nanowire structure, each axial segment was designed to grow for the same amount of time (12 min in this work), with the SiH_4 flow rate set to $3.1 \times 10^{-7}\,\mathrm{mol\,min}^{-1}$ for the doped segments and 0 for the undoped segment, targeting a nominal doping concentration profile of $\sim 1 \times 10^{18}\,\mathrm{cm}^{-3}$ and $< 1.5 \times 10^{17}\,\mathrm{cm}^{-3}$ respectively.

The n^+-i-n^+ InP nanowires were also characterized using the optical doping profiling technique [33] as shown in figure 2. The power-dependent PL spectra were measured point-by-point along the single n^+-i-n^+ nanowire. For each point, the TRPL intensity decay was recorded under the low excitation power condition [33] to extract a local PL lifetime for calculation of the doping concentration. A 'n'-shape PL spectrum peak position profile along the nanowire was

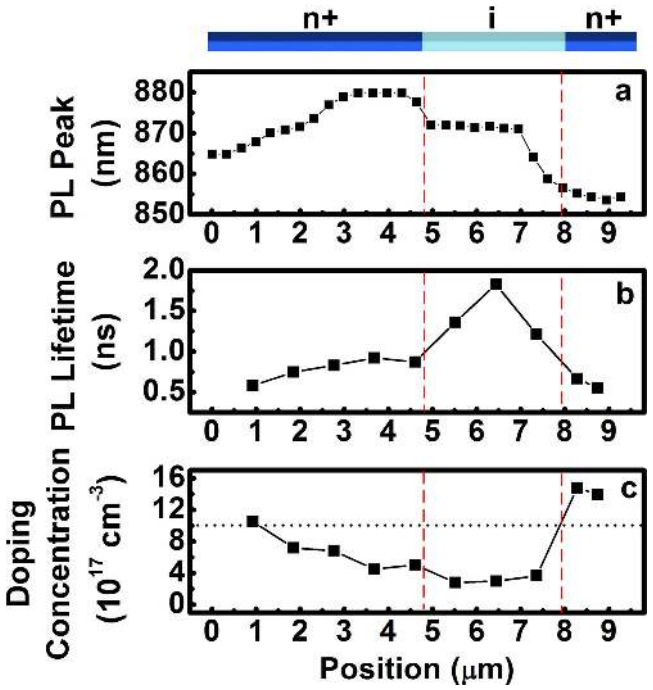

Figure 2. (a) PL spectrum peak position profile along a single n^+-i-n^+ InP nanowire studied in this work (position at 0 μm denotes the bottom of the nanowire where the growth starts). (b) The PL lifetime profile and (c) resulting doping profile along the same nanowire in (a). Dashed lines are guides for the eyes. Dotted line indicates the doping concentration of $10^{18}\,\mathrm{cm}^{-3}$.

observed (see figure 2(a)), where both ends show a blue-shift in PL peak position. This confirms that the ends of the nanowire have a relatively higher doping level, and that the doping is n-type [37], as designed. The PL lifetime profile along the same nanowire is shown in figure 2(b), indicating an asymmetric n^+-i-n^+ doping could have been formed within the InP nanowire. Figure 2(c) displays the resultant doping profile, as determined by our optical technique. It can clearly be seen that the doping along the nanowire is indeed asymmetrical, consistent with the PL lifetime profile. Nevertheless, the doping profile along the nanowire qualitatively follows the design of an n^+-i-n^+ structure, with dopant levels ranging from $0.28 \times 10^{18}\,\mathrm{cm}^{-3}$ to $1.48 \times 10^{18}\,\mathrm{cm}^{-3}$, from the nominally undoped section to heavily doped section, while the length of the undoped section is found to be ~3 μm, as expected. Some differences in length of the three sections was clearly observed and attributed to the growth rate variation with time during SA-MOVPE growth; it has previously been shown that SA-MOVPE InP nanowires grow faster near the base [38]. Considering the three sections in the n^+-i-n^+ nanowires were grown for the same duration of time in experiment, it can be inferred that the end starting from 0 on the abscissa in figures 2(a)–(c) is the base of nanowire. This end has a relatively lower doping and a smooth n^+-type to i-type doping profile, likely due to being held at a high temperature during growth for a longer time, leading to diffusion of the Si dopant from the base. The other end with shorter growth length is identified as the tip of the nanowire, which has higher doping and an abrupt doping profile next to

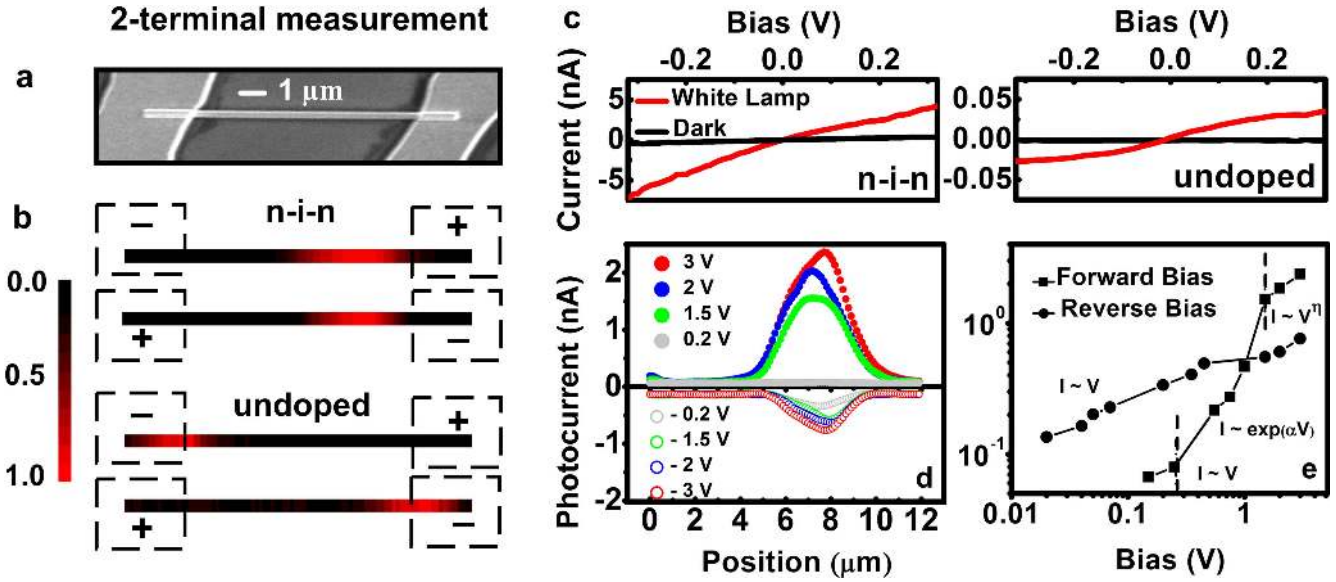

Figure 3. (a) A SEM image of a typical n^+-i-n^+ single InP nanowire device fabricated in this study. (b) The photocurrents along an n^+-i-n^+ (top) and an undoped (bottom) single InP nanowire device at biases of ±0.5 V scanned by a 532 nm continuous-wave laser with a spot size of ~720 nm (in diameter) and a scan step of 150 nm. The color from red to black in the mapping corresponds to the (normalized) photocurrent intensity from maximum to the minimum. (c) A comparison of *I–V* characteristics between an n^+-i-n^+ and an undoped single InP nanowire device under ambient (room light) illumination. (d) Bias-dependent photocurrents scanned along a single n^+-i-n^+ InP nanowire photodetector (under illumination from a 532 nm laser at a fluence of 49 mW cm^{-2} with a scan step of 150 nm). Positive bias means that the tip of the nanowire is positive relative to the base; accordingly, positive current means that the electron flows from the base towards the tip. (e) Photocurrent as a function of voltage on a log–log scale. The photocurrent data is extracted from the data in (d) at the position of ~7.7 μm (undoped region).

the undoped section. The analysis on the nanowire tip and base has also been confirmed by SEM imaging, where the tip end of the nanowire is easily identified by a flat surface profile and base end with a jagged profile (due to being broken off from the substrate [33]). In order to obtain a relatively symmetrical n^+-i-n^+ doping profile in the nanowire in the future, such deviations should be accounted for reducing growth time to minimize the dopant diffusion while providing a higher doping for n^+ region at the nanowire base. However, the current n^+-i-n^+ InP nanowires in this report meet the requirement for forming and investigating low-contact resistance nanowire devices.

To further characterize these n^+-i-n^+ InP nanowires, the photoconductivity lifetime and electron mobility of an ensemble of the n^+-i-n^+ InP nanowires were measured by time-domain optical pump-THz probe spectroscopy [18, 19] (details are provided in the online supplementary information). These parameters are crucial to evaluate the suitability of a semiconductor for THz detection: the photoconductivity lifetime determines the signal processing technique and noise level in the detector, while the carrier mobility determines its response level. We found that the incorporation of n^+ sections in the InP nanowires has a small influence on the original material conductivity properties. A ~1.91 ns photoconductivity lifetime was obtained for n^+-i-n^+ nanowires, comparable with ~1.71 ns measured for undoped ones. The electron mobility for n^+-i-n^+ InP nanowires was found to be approximately 950 ± 560 $cm^2\,V^{-1}\,s^{-1}$, also comparable with 1260 ± 320 $cm^2\,V^{-1}\,s^{-1}$ measured for undoped ones. The slight differences in both photoconductivity lifetime and electron mobility could be owing to the increased ionized impurity scattering in doped nanowires [39]. Despite that, they still indicate that a high material quality is maintained in the doped nanowires.

Based on the doping profile analysis, we fabricated Ti/Au electrodes on the n^+-i-n^+ single InP nanowire, intentionally covering each end with a metallized region of ~1 μm (the device geometry is provided in figure 3(a)). It was found in our case that a longer contact length (>2 μm) would overlap with the undoped section, reducing the active area of the resultant device; while shorter contact length (<800 nm long) would reduce the contact area to the nanowire device, introducing variability in the contact quality. In order to investigate the improvement of the contact resulting from the n^+-i-n^+ design, spatially-resolved photocurrent mapping of the single InP nanowire devices was performed using 532 nm continuous-wave laser excitation. Figure 3(b) shows the photocurrent distribution along both a single n^+-i-n^+ InP nanowire device and an undoped single InP nanowire device at biases of ±0.5 V. It can be seen that for the n^+-i-n^+ nanowire device, the photocurrent predominantly originates from the central, undoped i section of the nanowire; while for the undoped nanowire device, the photocurrent is mainly from the contact junctions (which can be described as having back-to-back Schottky contacts). This indicates that the n^+ sections of the n^+-i-n^+ nanowire worked well, as intended, lowering the contact barrier height, to form low-resistance contacts at both ends of the single nanowire device. It is also noted that the photocurrent profile along the n^+-i-n^+ single InP nanowire device is in good agreement with the doping

profiles shown in figures 2(a)–(c), confirming that the photocurrent in the n^+-i-n^+ single nanowire device mostly arises from the undoped i section. Importantly, the n^+-i-n^+ single nanowire device exhibits a strong photosensitivity even under room light illumination (figure 3(c)), whereas the undoped single nanowire device shows significantly lower photo-response under the same illumination condition (figure 3(d)). More quantitative comparisons of the photo-response between the n^+-i-n^+ and undoped single nanowire devices are provided in supporting information. Subsequently, power-dependent photocurrent measurements along the n^+-i-n^+ nanowire device were carried out (details are provided in supporting information), indicating that the non-metallized n^+ sections, which have a relatively low photosensitivity due to the free carrier absorption [40], also contribute to the total photocurrent. For optimized photo-detection, the length of the n^+ section in n^+-i-n^+ nanowires could be further minimized. In order to examine the influence of doping asymmetry observed in figure 2 on the device performance, bias-dependent photocurrent measurements along single n^+-i-n^+ nanowires were performed. It can be seen from figure 3(d) that the photocurrent from the n^+-i-n^+ device shows a distinct difference in intensity under positive and negative bias. However, the spatial origin of photocurrent is insensitive to the applied bias direction and always observed predominantly from the nominally undoped section.

The *I–V* characteristics for the n^+-i-n^+ nanowire device are plotted in figure 3(e). For the case of positive bias (the tip of the nanowire is positively relative to the base), the photocurrent increases with increasing bias voltage and can be described by three different carrier-transport regimes: (I) a linear behavior at the very low voltage region, obeying Ohm's law; (II) an exponential behavior at the medium voltage region, commonly occurring in the wide band gap p-n diodes due to a recombination tunneling mechanism [41, 42]; and (III) a power-law behavior at the high voltage region, resulting from space-charge-limited current [43]. The observation of the three regions indicate the presence of a large Schottky barrier under positive bias in the device. For the case of negative bias (the base of the nanowire is positively relative to the tip), only one behavior is observed: the photocurrent increases following a linear relationship, indicating a very low Schottky barrier (hence a quasi-Ohmic contact) in the device under negative bias. The different barrier heights indicated from the figure 3(e) can be ascribed to the difference in doping levels at the tip and the base of the n^+-i-n^+ InP nanowire. The contact at the base may be responsible for the higher barrier, as the base has a lower doping concentration due to diffusion effect (see figure 2(c)). These imperfect Ohmic contacts for current n^+-i-n^+ nanowire devices suggest that there is still room for further improvement of n^+-i-n^+ nanowire growth. Nevertheless, both contact barrier heights in the n^+-i-n^+ device have still been significantly reduced through contact doping, since the n^+-i-n^+ InP nanowire device shows a much higher photo-response than the undoped nanowire device under the same measurement condition. Furthermore, the n^+-i-n^+ InP nanowire device also presents a greatly improved sensitivity due to the improved contact quality, capable of low-voltage operation (at 0.1 V) over a wide temperature range from 77 to 300 K. Details of temperature-dependent photocurrent spectral response for the n^+-i-n^+ InP single nanowire device and related optical simulations regarding its spectral absorption characteristics are provided in supporting information.

Finally, the n^+-i-n^+ InP nanowires were fabricated into single-nanowire THz detectors with a strip-line electrode geometry [19], and were incorporated in a standard THz-TDS system for characterization. Details of the device fabrication and THz-TDS measurements are provided in the online supplementary information. Figures 4(a)–(f) shows typical THz responses obtained from an undoped InP single-nanowire detector, an n^+-i-n^+ InP single-nanowire detector, and a traditional (bulk) ion-implanted InP photoconductive detector in the THz-TDS system, with the same electrode geometry. The n^+-i-n^+ nanowire detector shows a broad spectral response bandwidth in the range of 0.1–2.2 THz with a good sensitivity and a low noise level, similar to the undoped nanowire detector and the traditional bulk detector. In our work, the detector bandwidth is defined as the cutoff frequency at the noise floor of its spectral response. The noise floor is related to the dark current of the detector, and therefore the Johnson–Nyquist noise is the dominant noise source in bulk detectors [19]. For single nanowire detectors, due to the nanoscale active material volume and the use of an insulating substrate, a significant reduction of Johnson–Nyquist noise and thus a low noise floor can be achieved. As a further demonstration of their functionality, the n^+-i-n^+ nanowire detectors were used to measure the refractive index (figure 4(g)) and absorption coefficient (figure 4(h)) of a piece of paper cards over a THz range from 0.5 to 1.5 THz in the THz-TDS system. The measured values using the n^+-i-n^+ nanowire detector are in good agreements with the literature [44, 45] as well as those obtained using a conventional (bulk ion-implanted InP) THz detector [19], demonstrating the practical value of the n^+-i-n^+ InP single-nanowire THz detectors.

Table 1 summarizes a detailed comparison of device performance among the undoped InP single-nanowire THz detector, n^+-i-n^+ InP single-nanowire THz detector and traditional ion-implanted InP THz detector. The spectral response bandwidths of the three types of THz detectors are comparable however with some marginal differences (traditional detector $\gtrsim$ n^+-i-n^+ nanowire detector $\gtrsim$ undoped nanowire detector). Since all experimental factors that influence the measured spectral bandwidth, such as the laser pulse duration, the THz source and the detector antenna geometry (a strip-line structure), are kept the same for all detectors, the difference in response bandwidth for the three detectors can be attributed to the difference in their noise floor level as shown in figures 4(b), (d) and (f)), signal-to-noise ratio [46] (defined as the average peak-to-peak current to the standard deviation of the difference of peak-to-peak current from two consecutive scans) and dynamic range [19, 47] (defined as the peak-to-peak current over one time-domain scan to the standard deviation of the noise current in the absence of THz over the same scan). As a direct result of the improved contact

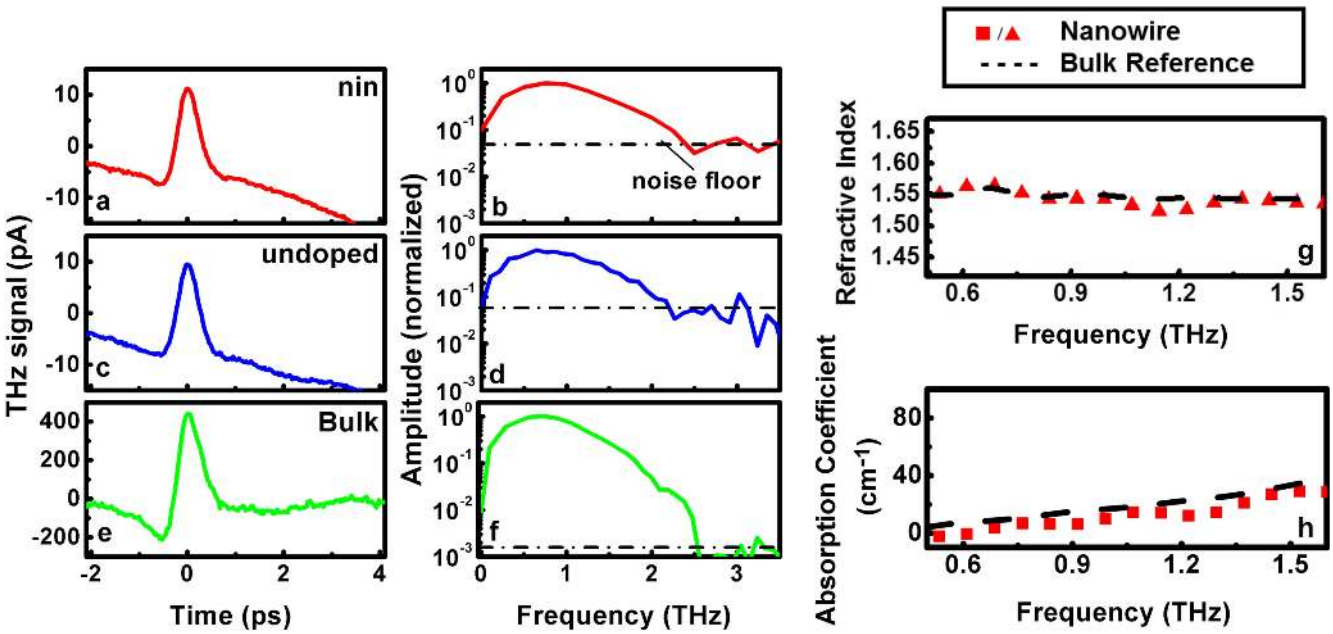

Figure 4. (a)–(f) THz responses measured from a typical n^+-i-n^+ InP single-nanowire detector (red, top), undoped InP single-nanowire detector (blue, middle) and a traditional ion-implanted InP detector (green, bottom) in a THz-TDS system. The noise floor is defined by averaging the random noise of each frequency spectrum. (b), (d) and (f) Calculated amplitude spectral responses obtained from (a), (c) and (e), respectively. Refractive index (g) and absorption coefficient (h) of a paper card obtained by characterization in the THz-TDS system using the n^+-i-n^+ nanowire detector and the traditional detector.

Table 1. Comparison of device performance between InP nanowire detector and traditional ion-implanted InP photoconductive detector. (For signal-to-noise ratio, the signal is defined as the peak-to-peak current over one time-domain scan, and the noise is the standard deviation of the difference of two consecutive scans with identical parameters. Dynamic range is defined as the ratio of the peak-to-peak current over one time-domain scan to the standard deviation of the noise current in the absence of THz over the same scan.)

	Detector type		
	Photoconductive antenna (strip lines)		
	InP single nanowire		InP bulk
Performance	Undoped	n-i-n	Ion-implanted
Spectral response bandwidth (THz)	2	2.2	2.5
Signal-to-noise ratio	21	53	70
Dynamic range	103	118	540
THz induced current (pA)	19.5	19.1	676.6

quality, the n^+-i-n^+ nanowire detector shows lower noise current fluctuation and a lower noise floor compared to the undoped nanowire detector, and exhibits an improved response bandwidth, signal-to-noise ratio and dynamic range. The signal-to-noise ratio of the n^+-i-n^+ nanowire detector increases by a factor of 2.5 to a value of 53 compared to the value of 21 of the undoped nanowire detectors. Although a significant difference in detection material volumes between the nanowire and bulk detector leads to a limited THz response current (a few tens of pA) and thus a 4–5 times reduction in dynamic range for the nanowire detectors, the n^+-i-n^+ nanowire detector still shows a comparable signal-to-noise ratio to the bulk detector, indicating that doping engineering is an effective and promising tool for optimization of single-nanowire THz devices.

We anticipate that further improvements in nanowire detector performance (for better signal-to-noise ratio and dynamic range) can be achieved through increasing the doping concentration of n^+ sections in the nanowire to achieve better Ohmic contacts, as well as performing a careful growth calibration to produce a longer i section to increase the THz response current. It is also noted that the peak value of the THz response current obtained for the n^+-i-n^+ nanowire detector is very close to that of the undoped nanowire detector; this is given the difference observed in above direct-current (DC) photocurrent measurements. Unlike the DC photocurrent measurement, which requires an external bias to produce a voltage drop across the contacts of device to drive the photo-induced electron-hole pairs to form a current, the photoconductive detector for THz measurement requires no external bias to be applied for operation. The incident THz electric field coupled into the detector acts as an ultrashort alternating-current (AC) bias to drive the photo-induced carriers to the contacts. For the former case, the response current is strongly dependent on contact quality, as non-Ohmic contact introduces a parasitic resistance to the current flow. For the latter, the photo-excited carrier density in the detection material determines the current flow, as THz electric field is distributed uniformly inside the detector and drives the current directly without voltage loss (in the contacts). However, it is important to achieve two Ohmic contacts in photoconductive THz detector, as Schottky contacts have been shown to lead to a THz rectification behavior [48]. It is noted

that rectification is highly non-linear, which can amplify small variations such as pulse-to-pulse or scan-to-scan noise, whereas Ohmic contacts are inherently linear leading to a more stable and accurate current response of the detector and thus higher detection sensitivity. Finally, it is worth mentioning that, the photoconductive detector may be further modified for use as a photoconductive emitter (to generate THz radiation) in THz-TDS. However, photoconductive THz generation is in a sense an opposite process to photoconductive detection, in which an externally applied DC bias is required for operation. The external bias field distribution inside the emitter with Schottky contact electrodes will be localized close to the contacts, which may largely limit the THz emission efficiency. Therefore, forming Ohmic contacts to obtain uniform bias field distribution is not only important for photoconductive THz detectors but also essential for photoconductive THz emitters for low-voltage [49] operation and high output powers.

In summary, we have performed a detailed study of n^+-i-n^+ InP single nanowires to achieve low-contact resistance photoconductive detectors for highly-sensitive THz detection. A novel and widely-applicable optical technique was used to profile the doping concentration along the nanowire for design and optimization of the n^+-i-n^+ nanowire structure. This approach can also be extended to study other axially-doped nanowire heterostructures, opening a new path to further improve nanowire-based devices for their practical development. Through doping engineering of InP nanowires, the contact quality in the device was significantly improved, leading to high-quality THz detection. The excellent detection capability of n^+-i-n^+ InP single-nanowire THz detectors further prove the suitability of using III–V nanowires to achieve nanoscale THz electronics for advanced THz systems for industrial/commercial THz applications. Future work will focus on new material development and optimization, device geometry/antenna design optimization, device fabrication reproducibility and integration of nanowire-based detectors for advanced THz-TDS systems.

Acknowledgments

We thank the Australian National Fabrication Facility (ANFF) ACT node for access to the epitaxy and fabrication facilities used in this work, the National Computational Infrastructure (NCI) for providing the computational resources for this work, and Bandwidth Foundry International Pty Ltd for their product service for this work. We also appreciate Dennis Gibson (ANU RSPE Electronics Unit), Fouad Karouta (ANFF), Kaushal Vora (ANFF) and Marco Zerbini (ENEA Frascati) for their helpful assistance with this work.

Author contributions

PP, LF, HHT, CJ and MBJ devised the study. KP carried out the nanowire characterization, device fabrication, and electrical measurements as well as THz-TDS measurements of the devices. QG grew and characterized the nanowires. QG and FW assisted with optical measurements of nanowires. ZYL carried out 4-terminal device fabrication and assisted with electrical measurements of devices. JB carried out the OPTP measurements. MBJ, JB and PP assisted with the THz-TDS measurements. SM performed the optical simulations (in the online supplementary information). KP, PP and LF prepared the manuscript. All authors discussed and commented on the manuscript.

Funding sources

The work is financially supported by the Australian Research Council (ARC) and the Engineering and Physical Sciences Research Council (EPSRC).

Competing financial interests

The authors declare that they have no competing financial interests.

References

[1] Jepsen P U, Cooke D G and Koch M 2011 Terahertz spectroscopy and imaging—modern techniques and applications *Laser Photon. Rev.* **5** 124–66
[2] Lloyd-Hughes J and Jeon T-I 2012 A review of the terahertz conductivity of bulk and nano-materials *J. Infrared Millim. Terahertz Waves* **33** 871–925
[3] Zeitler J A, Taday P F, Newnham D A, Pepper M, Gordon K C and Rades T 2007 Terahertz pulsed spectroscopy and imaging in the pharmaceutical setting—a review *J. Pharmacy Pharmacol.* **59** 209–23
[4] Markelz A, Roitberg A and Heilweil E J 2000 Pulsed terahertz spectroscopy of DNA, bovine serum albumin and collagen between 0.1 and 2.0 THz *Chem. Phys. Lett.* **320** 42–8
[5] Banerjee D, Von Spiegel W, Thomson M, Schabel S and Roskos H 2008 Diagnosing water content in paper by terahertz radiation *Opt. Express* **16** 9060–6
[6] Shen Y, Lo T, Taday P, Cole B, Tribe W and Kemp M 2005 Detection and identification of explosives using terahertz pulsed spectroscopic imaging *Appl. Phys. Lett.* **86** 241116
[7] Liu H-B, Zhong H, Karpowicz N, Chen Y and Zhang X-C 2007 Terahertz spectroscopy and imaging for defense and security applications *Proc. IEEE* **95** 1514–27
[8] Auston D H 1975 Picosecond optoelectronic switching and gating in silicon *Appl. Phys. Lett.* **26** 101–3
[9] Salem B, Morris D, Aimez V, Beerens J, Beauvais J and Houde D 2005 Pulsed photoconductive antenna terahertz sources made on ion-implanted GaAs substrates *J. Phys.: Condens. Matter* **17** 7327–33
[10] Kono S, Tani M, Gu P and Sakai K 2000 Detection of up to 20 THz with a low-temperature-grown GaAs photoconductive antenna gated with 15 fs light pulses *Appl. Phys. Lett.* **77** 4104–6
[11] Tani M, Matsuura S, Sakai K and Nakashima S-I 1997 Emission characteristics of photoconductive antennas based on low-temperature-grown GaAs and semi-insulating GaAs *Appl. Opt.* **36** 7853–9
[12] Wood C, Cunningham J, Hunter I, Tosch P, Linfield E and Davies A 2006 On-chip pulsed terahertz systems and their applications *Int. J. Infrared Millim. Waves* **27** 557–69
[13] Cunningham J, Byrne M, Wood C and Dazhang L 2010 On-chip terahertz systems for spectroscopy and imaging *Electron. Lett.* **46** s34–7
[14] Dasgupta N P, Sun J, Liu C, Brittman S, Andrews S C, Lim J, Gao H, Yan R and Yang P 2014 25th anniversary article: semiconductor nanowires—synthesis, characterization, and applications *Adv. Mater.* **26** 2137–84

[15] Vitiello M S, Coquillat D, Viti L, Ercolani D, Teppe F, Pitanti A, Beltram F, Sorba L, Knap W and Tredicucci A 2012 Room-temperature terahertz detectors based on semiconductor nanowire field-effect transistors *Nano Lett.* **12** 96–101

[16] Romeo L, Coquillat D, Pea M, Ercolani D, Beltram F, Sorba L, Knap W, Tredicucci A and Vitiello M S 2013 Nanowire-based field effect transistors for terahertz detection and imaging systems *Nanotechnology* **24** 214005

[17] Vitiello M S, Viti L, Coquillat D, Knap W, Ercolani D and Sorba L 2015 One dimensional semiconductor nanostructures: an effective active-material for terahertz detection *APL Mater.* **3** 026104

[18] Peng K *et al* 2015 Single nanowire photoconductive terahertz detectors *Nano Lett.* **15** 206–10

[19] Peng K *et al* 2016 Broadband phase-sensitive single InP nanowire photoconductive terahertz detectors *Nano Lett.* **16** 4925–31

[20] Castro-Camus E, Lloyd-Hughes J, Fu L, Tan H H, Jagadish C and Johnston M B 2007 An ion-implanted InP receiver for polarization resolved terahertz spectroscopy *Opt. Express* **15** 7047–57

[21] Li M, Sun F G, Wagoner G A, Alexander M and Zhang X C 1995 Measurement and analysis of terahertz radiation from bulk semiconductors *Appl. Phys. Lett.* **67** 25–27

[22] Hobbs R G, Petkov N and Holmes J D 2012 Semiconductor nanowire fabrication by bottom-up and top-down paradigms *Chem. Mater.* **24** 1975–91

[23] Shi W, Hou L and Wang X 2011 High effective terahertz radiation from semi-insulating-GaAs photoconductive antennas with ohmic contact electrodes *J. Appl. Phys.* **110** 023111

[24] Mikulics M, Marso M, Wu S, Fox A, Lepsa M, Grutzmacher D, Sobolewski R and Kordos P 2008 Sensitivity enhancement of metal–semiconductor–metal photodetectors on low-temperature-grown GaAs using alloyed contacts *IEEE Photon. Technol. Lett.* **20** 1054–6

[25] Baca A, Ren F, Zolper J, Briggs R and Pearton S 1997 A survey of ohmic contacts to III–V compound semiconductors *Thin Solid Films* **308** 599–606

[26] Vieweg N, Mikulics M, Scheller M, Ezdi K, Wilk R, Hübers H-W and Koch M 2008 Impact of the contact metallization on the performance of photoconductive THz antennas *Opt. Express* **16** 19695–705

[27] Yu H J, McCarthy L, Xing H, Waltereit H, Shen L, Keller S, Denbaars S P, Speck J S and Mishra U K 2004 Dopant activation and ultralow resistance ohmic contacts to Si-ion-implanted GaN using pressurized rapid thermal annealing *Appl. Phys. Lett.* **85** 5254–6

[28] Zamdmer N, Hu Q, McIntosh K A and Verghese S 1999 Increase in response time of low-temperature-grown GaAs photoconductive switches at high voltage bias *Appl. Phys. Lett.* **75** 2313–5

[29] Mikulics M, Wu S, Marso M, Adam R, Forster A, Van Der Hart A, Kordos P, Luth H and Sobolewski R 2006 Ultrafast and highly sensitive photodetectors with recessed electrodes fabricated on low-temperature-grown GaAs *IEEE Photon. Technol. Lett.* **18** 820–2

[30] Broom R, Meier H and Walter W 1986 Doping dependence of the Schottky-barrier height of Ti-Pt contacts to n-gallium arsenide *J. Appl. Phys.* **60** 1832–3

[31] González-Posada F, Songmuang R, Den Hertog M and Monroy E 2011 Room-temperature photodetection dynamics of single GaN nanowires *Nano Lett.* **12** 172–6

[32] González-Posada F, Songmuang R, Den Hertog M and Monroy E 2013 Environmental sensitivity of n-i-n and undoped single GaN nanowire photodetectors *Appl. Phys. Lett.* **102** 213113

[33] Wang F, Gao Q, Peng K, Li Z, Li Z Y, Guo Y N, Fu L, Smith L M, Tan H H and Jagadish C 2015 Spatially resolved doping concentration and nonradiative lifetime profiles in single Si-Doped InP nanowires using photoluminescence mapping *Nano Lett.* **15** 3017–23

[34] Gao Q *et al* 2014 Selective-area epitaxy of pure wurtzite InP nanowires: high quantum efficiency and room-temperature lasing *Nano Lett.* **14** 5206–11

[35] Yoshikazu T, Soichiro A, Susumu N and Akio S 1990 Characterization of InP grown by OMVPE using tertiary-butylphosphine for the phosphorous source *Japan. J. Appl. Phys.* **29** 11–18

[36] Rigutti L, Bugallo A D, Tchernycheva M, Jacopin G, Julien F H, Cirlin G, Patriarche G, Lucot D, Travers L and Harmand J C 2009 Si incorporation in InP nanowires grown by Au-assisted molecular beam epitaxy *J. Nanomater.* **2009** 435451

[37] Bugajski M and Lewandowski W 1985 Concentration-dependent absorption and photoluminescence of n-type InP *J. Appl. Phys.* **57** 521–30

[38] Mandl B, Stangl J, Hilner E, Zakharov A A, Hillerich K, Dey A W, Samuelson L, Bauer G, Deppert K and Mikkelsen A 2010 Growth mechanism of self-catalyzed group III–V nanowires *Nano Lett.* **10** 4443–9

[39] Boland J L, Casadei A, Tütüncüoglu G Z, Matteini F, Davies C L, Jabeen F, Joyce H J, Herz L M, Fontcuberta i Morral A and Johnston M B 2016 Increased photoconductivity lifetime in GaAs nanowires by controlled n-type and p-type doping *ACS Nano* **10** 4219–27

[40] Walukiewicz W, Lagowski J, Jastrzebski L, Rava P, Lichtensteiger M, Gatos C and Gatos H 1980 Electron mobility and free-carrier absorption in InP; determination of the compensation ratio *J. Appl. Phys.* **51** 2659–68

[41] Fedison J B, Chow T P, Lu H and Bhat I B 1998 Electrical characteristics of magnesium-doped gallium nitride junction diodes *Appl. Phys. Lett.* **72** 2841–3

[42] Kumar M, Bhat T N, Rajpalke M K, Roul B, Kalghatgi A T and Krupanidhi S B 2011 Transport and infrared photoresponse properties of InN nanorods/Si heterojunction *Nanoscale Res. Lett.* **6** 609

[43] Ghosh R and Basak D 2007 Electrical and ultraviolet photoresponse properties of quasialigned ZnO nanowires/p-Si heterojunction *Appl. Phys. Lett.* **90** 243106

[44] Hattori T, Kumon H and Tamazumi H 2010 Terahertz spectroscopic characterization of paper *35th Int. Conf. on Infrared, Millimeter, and Terahertz Waves (Irmmw-Thz 2010)*

[45] Hussain B, Nawaz M, Ahmed M and Raja M Y A 2013 Measurement of thickness and refractive index using femtosecond and terahertz pulses *Laser Phys. Lett.* **10** 055301

[46] Castro-Camus E, Fu L, Lloyd-Hughes J, Tan H H, Jagadish C and Johnston M B 2008 Photoconductive response correction for detectors of terahertz radiation *J. Appl. Phys.* **104** 053113

[47] Naftaly M and Dudley R 2009 Methodologies for determining the dynamic ranges and signal-to-noise ratios of terahertz time-domain spectrometers *Opt. Lett.* **34** 1213–5

[48] Que C T, Tani M, Miyamaru F and Hangyo M 2005 Detection of THz radiation with Schottky photoconductive antenna *2005 Joint 30th Int. Conf. on Infrared and Millimeter Waves and 13th Int. Conf. on Terahertz Electronics* vol 2 pp 628–9

[49] Sheu J-K, Tsai J, Shei S-C, Lai W-C, Wen T-C, Kou C, Su Y-K, Chang S-J and Chi G-C 2001 Low-operation voltage of InGaN-GaN light-emitting diodes with Si-doped $In_{0.3}Ga_{0.7}N$/GaN short-period superlattice tunneling contact layer *IEEE Electron Device Lett.* **22** 460–2